Noninvasive [89]Zr-Transferrin PET Shows Improved Tumor Targeting Compared with ^{18}F-FDG PET in MYC-Overexpressing Human Triple-Negative Breast Cancer

Kelly E. Henry[1], Thomas R. Dilling[1], Dalya Abdel-Atti[1], Kimberly J. Edwards[1], Michael J. Evans[2], and Jason S. Lewis[1,3–5]

[1]Department of Radiology, Memorial Sloan Kettering Cancer Center, New York, New York; [2]Department of Radiology and Biomedical Imaging, University of California San Francisco, San Francisco, California; [3]Molecular Pharmacology Program, Memorial Sloan Kettering Cancer Center, New York, New York; [4]Department of Pharmacology and Radiology, Weill Cornell Medical College, New York, New York; and [5]Radiochemistry and Molecular Imaging Probes Core, Memorial Sloan Kettering Cancer Center, New York, New York

The current standard for breast PET imaging is ^{18}F-FDG. The heterogeneity of ^{18}F-FDG uptake in breast cancer limits its utility, varying greatly among receptor status, histopathologic subtypes, and proliferation markers. ^{18}F-FDG PET often exhibits nonspecific internalization and low specificity and sensitivity, especially with tumors smaller than 1 cm^3. MYC is a protein involved in oncogenesis and is overexpressed in triple-negative breast cancer (TNBC). Increased surface expression of transferrin receptor (TfR) is a downstream event of MYC upregulation and has been validated as a clinically relevant target for molecular imaging. Transferrin labeled with [89]Zr has successfully identified MYC status in many cancer subtypes preclinically and been shown to predict response and changes in oncogene status via treatment with small-molecule inhibitors that target MYC and PI3K signaling pathways. We hypothesized that [89]Zr-transferrin PET will noninvasively detect MYC and TfR and improve upon the current standard of ^{18}F-FDG PET for MYC-overexpressing TNBC. **Methods:** In this study, [89]Zr-transferrin and ^{18}F-FDG imaging were compared in preclinical models of TNBC. TNBC cells (MDA-MB-157, MDA-MB-231, and Hs578T) were treated with bromodomain-containing protein 4 (BRD4) inhibitors JQ1 and OTX015 (0.5–1 μM). Cell proliferation, gene expression, and protein expression were assayed to explore the effects of these inhibitors on MYC and TfR. **Results:** Head-to-head comparison showed that [89]Zr-transferrin targets TNBC tumors significantly better ($P < 0.05$–0.001) than ^{18}F-FDG through PET imaging and biodistribution studies in MDA-MB-231 and MDA-MB-157 xenografts and a patient-derived xenograft model of TNBC. c-Myc and *TfR* gene expression was decreased upon treatment with BRD4 inhibitors and *c-MYC* small interfering RNA ($P < 0.01$–0.001 for responding cell lines), compared with vehicle treatment. MYC and TfR protein expression, along with receptor-mediated internalization of transferrin, was also significantly decreased upon drug treatment in MDA-MB-231 and MDA-MB-157 cells ($P < 0.01$–0.001). **Conclusion:** [89]Zr-transferrin targets human TNBC primary tumors significantly better than ^{18}F-FDG, as shown through PET imaging and biodistribution studies. [89]Zr-transferrin is a useful tool to interrogate MYC via TfR-targeted PET imaging in TNBC.

Key Words: triple-negative breast cancer (TNBC); positron emission tomography (PET); zirconium-89 ([89]Zr); ^{18}F-fluorodeoxyglucose (^{18}F-FDG); MYC; transferrin receptor (TfR); bromodomain-containing protein 4 (BRD4)

Estrogen, progesterone, and HER2/neu receptor–negative triple-negative breast cancers (TNBCs) encompass the most clinically challenging subtype, for which targeted therapeutics and molecular imaging modalities are lacking (*1*). There is evidence that TNBC tumors exhibit elevated MYC expression and altered expression of MYC regulatory genes, resulting in increased activity of the MYC pathway (*1,2*). About 20% of all breast cancers are classified as triple-negative, and about 75% of those include the basal-like subtype (*3*), in which MYC is a key driver (*4*). Although MYC has been shown to alter metabolism in tumorigenesis, it has a largely unknown specific role in TNBC metabolism (*5*), but is often associated with poor prognosis (*1*).

In contrast to normal cells, cancer cells fervently take up glucose and metabolize it to lactate even if oxygen is available (*6*). This process within cancer is known as the Warburg effect, which is a vital change in glucose metabolism that enables detection of cancer by PET imaging via intravenous injection of the glucose analog ^{18}F-FDG (*6–8*). ^{18}F-FDG is the most widely used PET agent for tumor imaging because cancer cells have higher glucose uptake than normal cells and ^{18}F can be readily assimilated into glucose to mimic the biology of the sugar (*9*). The overwhelming issue with ^{18}F-FDG PET for breast imaging is nonspecific internalization of the probe due to non–cancer-related glucose uptake, resulting in false-positive findings of malignancy (*10–13*).

This imaging technique is also limited by the fact that not all cancers avidly take up ^{18}F-FDG (*14*), and the heterogeneity of breast cancer also contributes to this issue (*15*). Although ^{18}F-FDG is the most commonly used PET tracer in the clinic, the relationship between its uptake in tumors and changes in metabolic, gene, and protein effectors is not well understood (*16*). An additional caveat of ^{18}F-FDG is that this tracer can be avid for postsurgical inflammation, which can result in false-positive findings for nonmalignant regions of the breast (*13,17*). ^{18}F-FDG has been used to detect early metabolic response to neoadjuvant chemotherapy but cannot usually

discriminate partial from total response—an ability that is critical for determining prognosis (18). ^{18}F-FDG is neither sensitive nor specific for lesions smaller than 1 cm[3], resulting in further limitations of this radiotracer (19) in the clinical setting. Also, the spatial resolution of ^{18}F-FDG PET can be a limiting factor for diagnosis, especially in the context of breast cancer (20). There have been case reports of misinterpretation of ^{18}F-FDG scans, such as sarcoid masses and other disease that were mistaken for malignancy (21). The histologic subtype needs to be carefully considered when interpreting ^{18}F-FDG uptake in metastatic disease, especially within the realm of breast cancer (22).

There is a literature precedent that MYC-overexpressing basal-like TNBC is avid for ^{18}F-FDG (7). Palaskas et al. performed a widespread transcriptional exploration of breast cancer tumors to confirm these effects, identifying many genes, including transferrin receptor (TfR), that could be important to assess the heterogeneity of these tumors (7). Although MYC is a well-established protein in oncogenesis, it is also a key regulator of multiple downstream oncogenic pathways, including TfR. Cancer cells generally express higher levels of TfR than normal cells, likely to facilitate the increase in Fe^{3+} necessary for biologic processes associated with cell proliferation (23,24). Alterations in iron metabolism within the tumor microenvironment may also facilitate breast tumor growth (25), and expression of iron metabolic genes in breast tumors is predictive of breast cancer prognosis (26). Targeting TfR has been of interest as a therapeutic strategy for both treatment and imaging, particularly in developing tools for noninvasive TfR imaging, as it is upregulated on the surface of many cancer types and is efficiently internalized (24,27). We previously showed that TfR has been established as a clinically relevant target for imaging in MYC-driven models of prostate cancer, hepatocellular carcinoma, and lymphoma (24,27–29). Investigational new drug–enabling studies have been completed—to continue to first-in-human imaging studies for [89]Zr-transferrin—and will commence in prostate cancer patients later this year. In breast cancer, detection of surrogate biomarkers in the neoadjuvant setting is optimal for prediction of pathologic response, which could allow TfR as a biomarker to be of significant clinical benefit.

The research described within this article incorporates ^{18}F-FDG and [89]Zr-transferrin PET for noninvasive targeting of MYC and TfR in vivo and interrogation of treatment response by bromodomain-containing protein 4 (BRD4) inhibitors in vitro. We hypothesized that [89]Zr-transferrin PET will noninvasively detect overexpression of MYC and TfR and serve as a superior alternative to ^{18}F-FDG PET for MYC-overexpressing TNBC.

MATERIALS AND METHODS

Cell Lines and BRD4 Inhibitors

TNBC cell lines (MDA-MB-231, MDA-MB-157, and Hs578T) were obtained from the American Type Culture Collection. All cells were grown according to the recommendations of the manufacturer under 37°C with 5% CO_2 in a humidified atmosphere. All tissue culture manipulations were performed using sterile techniques. TNBC cells were treated with JQ1 (ApexBio) and OTX015 (Cayman Chemical) at 0.5–1 μM. All BRD4 inhibitors were confirmed to be more than 99% pure via in-house quality control assessment.

Cell Cycle Analysis

To confirm the antiproliferative effects of BRD4 inhibitors in TNBC cells and determine the point of cellular arrest, a flow cytometry assay using 5-ethynyl-2′-deoxyuridine (EdU) incorporation was performed. TNBC cells were seeded in 6-well plates (5×10^5) and incubated at 37°C with 5% CO_2 in a humidified atmosphere overnight. Cells were incubated with fresh medium, medium with 0.5–1 μM drug (JQ1 or OTX015), or vehicle control (dimethyl sulfoxide [DMSO] at matching concentrations) for 24 h. After drugging, EdU (10 μM) was added directly to the cells (without disruption) and incubated for 1 h at 37°C. Cells were immediately harvested and washed twice with cold phosphate-buffered saline (PBS) and incubated with LIVE/DEAD (Thermo Fisher Scientific) fixable viability dye (488-nm excitable), which can withstand the fixing process required for this protocol. Cells were then subjected to the Click-iT (Thermo Fisher Scientific) EdU system protocol for staining with Alexa Fluor 647 (Thermo Fisher Scientific), which, combined with 4′,6-diamidino-2-phenylindole (3.6 μM), was used to resolve cell cycle phases in a given population into G_0/G_1, S, and G_2/M. Nonviable cells were gated out with the 488-nm excitable LIVE/DEAD fixable viability stain, and data were analyzed by FlowJo software and plotted using Prism (GraphPad).

Western Blot

TNBC cells were plated in 100-mm culture dishes at 3×10^6 cells per dish. Cells were incubated with fresh medium with vehicle (DMSO) or drug (0.5 μM JQ1 and OTX015) and incubated for 24, 48, and 72 h. Cells were harvested and chemically lysed with radioimmunoprecipitation assay buffer with protease inhibitor cocktail and phosphatase inhibitors (1:100 dilution for each inhibitor; EMD Millipore). Cells were then subjected to mechanical lysis via sonication pulses at 4°C (10 s on, 10 s off) for 10 min. Cell debris was then pelleted via centrifugation at 14,000 rpm. The supernatant was analyzed for total protein content using a Lowry assay with a bovine serum albumin standard curve. Lysates were prepared at a 2 μg/mL total protein content with 4× sodium dodecyl sulfate polyacrylamide gel electrophoresis loading dye, boiled for 5 min at 95°C, and stored at −20°C until use. Samples were loaded onto 7% tris-acetate gels and subjected to dry transfer via iBlot (Thermo Fisher Scientific) to nitrocellulose membranes. Ponceau red (0.5% w/v) was used to confirm protein transfer, and membranes were blocked in 5% nonfat dry milk in Tris-buffered saline with 0.1% polysorbate for 1 h at room temperature. Blots were then incubated overnight with primary antibodies (anti-MYC: clone D84C12, 500:1 dilution [Cell Signaling Technology Inc.]; anti-CD71: clone D7S5Z, 1,000:1 dilution [Cell Signaling Technology Inc.]; anti-β-actin, clone AC-15, 20,000:1 dilution [Sigma-Aldrich]) at 4°C in blocking solution. Blots were incubated with horseradish peroxidase–conjugated secondary antibodies (antimouse: catalog no. ab6789, 7,500:1 dilution; antirabbit: catalog no. ab6721, 5,000:1 dilution [Abcam]) for 1 h at room temperature. Bands were detected using enhanced chemiluminescent signal substrate (GE Healthcare).

Quantitative Reverse-Transcriptase Polymerase Chain Reaction (RT-PCR)

Quantitative RT-PCR was performed to quantify relative c-Myc and TfR (CD71) gene expression levels before and after treatment with BRD4 inhibitors, normalized to housekeeping gene expression (glyceraldehyde-3-phosphate dehydrogenase, or GAPDH). Cells were plated in 12-well plates at 3×10^5/mL, allowed to adhere overnight, and incubated with fresh medium with vehicle (DMSO) or drug (0.5–1 μM JQ1 and OTX015). From the collected cell pellets, cells were lysed using QIAShredder (QIAGEN), and messenger RNA (mRNA) was extracted using an RNeasy isolation kit (QIAGEN). Isolated mRNA was converted to complementary DNA using 1 μg of mRNA product and a high-capacity complementary DNA conversion reverse transcriptase kit (Applied Biosystems) with random primers. Aliquots of complementary DNA were quantified and prepared for triplicate reactions in a quantitative RT-PCR plate using TaqMan fast advanced master mix and c-Myc (assay no. Hs00153408; Applied Biosystems) and TfR (CD71) TaqMan polymerase gene assays (assay no. Hs00951083; Applied Biosystems). Data were normalized with respective housekeeping

genes (GAPDH, assay no. Hs03929097; Applied Biosystems); no template controls were included as negative controls.

Flow Cytometry

Flow cytometry used a phycoerythrin-labeled anti-CD71 (TfR) antibody (clone CY1G4; BioLegend) to assess surface TfR protein levels before and after drug treatment with BRD4 inhibitors in TNBC cells. Cells were plated in 6-well plates at 3×10^5/mL, allowed to adhere overnight, and incubated with fresh medium with vehicle (DMSO) or drug (0.5–1 μM JQ1 and OTX015) for 48 h. After incubation, the cells were washed twice with PBS, trypsinized, and centrifuged to collect pellets. The cells were resuspended in Fc receptor–blocking solution (Miltenyi Biotec) for 30 min to prepare for surface antigen staining (TfR) and analyzed via flow cytometry. 4′,6-diamidino-2-phenylindole was used as a viability marker for surface-staining experiments. A phycoerythrin-labeled IgG (clone MOPC-173; BioLegend) was used as an isotype control to confirm specific binding to CD71 in TNBC cells. Data were analyzed by FlowJo software and plotted using Prism (GraphPad).

Small Interfering RNA (siRNA) Transfection

TNBC cells were seeded in 12-well plates at 1×10^5 cells per well in antibiotic-free medium and incubated overnight. Dharmafect siRNA (c-MYC, 50 nM; Dharmacon) was administered to TNBC cells in antibiotic-free medium. Nontargeted siRNA pool was also administered at matching concentrations, along with untreated cells and GAPDH-targeted siRNA as controls. Quantitative RT-PCR was performed to quantify relative c-Myc and TfR (CD71) gene expression levels before and after treatment as described above. Protein analysis was performed via western blot using the same protocol as described above.

Internalization Assays with BRD4 Inhibitors

Holo-transferrin (2 mg) was labeled with ^{131}I (74 MBq) using Iodo-Gen (Pierce Biotechnology, Inc.) activation for 15 min in PBS. Purification was accomplished in a 30-kDa molecular-weight-cutoff Amicon (Merck) filter column with 3 washes in PBS (pH 7.4). Transferrin labeling was assessed via instant thin-later chromatography with a mobile phase of 10% trifluoroacetic acid to detect any ^{131}I not incorporated into the protein. Cells were plated at 3×10^5/mL, allowed to adhere, and incubated with fresh medium with vehicle (DMSO) or drug (0.5 μM JQ1 and OTX015) for 48 h. The radiochemical yield for each experiment was greater than 95%, and radiochemical purity was 99%. Cells were incubated with fresh medium or medium with ^{131}I-transferrin (0.037 MBq/well) for 1 h at 37°C. Media (with or without radiotracer) was removed, and the cells were washed twice with PBS and trypsinized. Duplicate plates were used and treated the same for both protein quantification (for data normalization) and γ-counting.

Preparation and Radiolabeling of ^{89}Zr-DFO-Transferrin

Apo-transferrin was functionalized with p-isothiocyanatobenzyl-desferrioxamine (Macrocyclics, Inc.) and characterized to have 1 chelate per protein molecule via isotopic dilution assay (30). The desferrioxamine-modified protein was purified via a PD10 desalting column (GE Healthcare). The precursor was manufactured using good manufacturing processes and obtained from the Radiochemistry and Molecular Imaging Probes Core at Memorial Sloan Kettering Cancer Center. ^{89}Zr was produced through proton-beam bombardment of yttrium foil and isolated in high purity as ^{89}Zr-oxalate at Memorial Sloan Kettering Cancer Center according to a previously published procedure (30). ^{89}Zr-oxalate (37 MBq) was neutralized to pH 7.0–7.4 with 1 M Na$_2$CO$_3$. The desferrioxamine-transferrin was added (100 μg), and the reaction was incubated at room temperature for 1 h. Subsequent purification was conducted using a PD10 desalting column with PBS. Purity and radiolabeling yields were quantified through instant thin-later chromatography with a 50 mM ethylenediaminetetraacetic acid (pH 5) mobile phase.

Internalization Assays: Time Course

Transferrin was radiolabeled with ^{89}Zr as described above. TNBC cells were incubated with fresh medium or medium with ^{89}Zr-transferrin (0.037 MBq/well) at 37°C, with samples collected at multiple time points (15, 30, 45, 60, and 90 min). Media (with radiotracer) was removed at multiple time points, and the cells were washed twice with PBS, rinsed with 100 mM acetic acid and 100 mM glycine (pH 3) to remove surface-bound tracer, and lysed with 1 M NaOH to collect the internalized fraction. Duplicate plates were used and treated the same for both cell counting (for data normalization) and γ-counting.

Small-Animal Models

All animal studies were conducted in accordance with the guidelines set by the Institutional Animal Care and Use Committee. Female athymic nude (nu/nu) mice (6–8 wk old, 20–22 g) were inoculated with TNBC tumors. Cells were implanted orthotopically (5×10^6 cells) in the lower right mammary fat pad in 50 μL of 1:1 Matrigel (BD Biosciences) and grown to a tumor volume of 150–200 mm^3 before use.

Patient-Derived Xenografts

The TNBC patient-derived xenograft model (M24) was a kind gift from the Baselga Lab at Memorial Sloan Kettering Cancer Center and was inoculated subcutaneously on the flank in a suspension with Matrigel (1:1).

^{18}F-FDG Imaging

^{18}F-FDG was obtained from the Nuclear Pharmacy at Memorial Sloan Kettering Cancer Center on the morning of injection (13–15 MBq/injection). ^{18}F-FDG was acquired from Zevacor Molecular, and the specific activity ranged from 0.74 to 11.1 GBq/mL at the end of synthesis. The mice were kept fasting overnight and anesthetized with 1.5%–2% isoflurane (Baxter Healthcare) for 30 min before PET imaging. All mice were imaged at 1 h after injection.

In Vivo Imaging

The mice were anesthetized with 1.5%–2% isoflurane (Baxter Healthcare) in oxygen. PET imaging experiments were accomplished with a microPET Focus 120 scanner (Concorde Microsystems). The mice were administered ^{89}Zr-labeled transferrin (9–11 MBq, 80 μg) in 150–200 μL of 1× PBS formulations via lateral tail vein injections. PET whole-body acquisitions were recorded at 4–48 h after injection while the mice were anesthetized with 1.5%–2.0% isoflurane in oxygen. The images were analyzed using ASIPro VM software (Concorde Microsystems).

Biodistribution Studies

Biodistribution studies were performed to measure the uptake of the radioconjugate in tumor and other relevant organs and tissues. After each time point, mice were euthanized by asphyxiation with CO$_2$. Blood was collected immediately via cardiac puncture while the tumor along with chosen organs was harvested. The wet weights of each tissue were calculated, and the radioactivity bound to each organ was counted using standard γ-counters. The percentage of tracer uptake expressed as percentage injected dose per gram was calculated as the activity bound to the tissue per organ weight per actual injected dose decay-corrected to the time of counting.

Autoradiography and Histology

After PET imaging and biodistribution studies, a subset of tumors was embedded in optimal-cutting-temperature mounting medium and frozen on dry ice. Series of 10-μm frozen sections were then sliced at multiple tumor levels. To determine radiotracer distribution, digital autoradiography was performed by placing tissue sections in a film

cassette against a phosphor imaging plate (Fujifilm BAS-MS2325; Fuji Photo Film) for an appropriate exposure period at $-20°C$ (10 min for ^{18}F-FDG, and 96 h for ^{89}Zr-transferrin). Phosphor imaging plates were read at a pixel resolution of 25 μm with a Typhoon 7000 IP plate reader (GE Healthcare). After autoradiographic exposure, the same frozen sections were then used for immunohistochemical staining and microscopy. Immunohistochemical staining of TfR and c-MYC was performed using antibodies (abcam), along with TfR blocking peptide (abcam) as a control (anti-c-MYC [Y69] ab32072, 10 μg/mL; anti-TfR ab84036, 4 μg/mL; human transferrin receptor peptide ab101219, 10× excess), on both paraffin-embedded tissue (tumors fixed in neutral-buffered formalin on excision) and fresh-frozen tissue (same tissue as used for autoradiography). Sequential sections were stained with hematoxylin–eosin. Immunohistochemical and autoradiographic images were registered using Pannoramic Viewer and Fiji, respectively.

Statistical Considerations

Tumor uptake was determined from both biodistribution studies as previously described or from the regions of interest drawn from acquired PET images using ASIPro image analysis software (Siemens). The results for the drawn regions of interest were expressed as the average percentage injected dose per gram. All data were analyzed by the unpaired, 2-tailed Student t test, and differences at the 95% confidence level ($P < 0.05$) were considered statistically significant. Positive and negative controls were included whenever possible.

RESULTS

Interrogating the Effects of BRD4 Inhibitors on MYC and TfR In Vitro

To study the pharmacologic MYC-mediated effects of TfR in vitro, BRD4 inhibitors were administered to TNBC cells at nanomolar–low micromolar concentrations (31). Multiple experiments showed a response of BRD4 inhibitors in TNBC cells with regard to proliferation, gene expression, and protein expression. TNBC cells (MDA-MB-231, MDA-MB-157, and Hs578T) showed

a significant ($P < 0.05$–0.001) antiproliferative response to JQ1 and OTX015 at a nanomolar range via EdU incorporation as a proliferation marker (Supplemental Fig. 1; supplemental materials are available at http://jnm.snmjournals.org). The percentage of cells in S phase was significantly decreased, confirming cell cycle arrest at the G_0/G_1 phase upon drug treatment, as is consistent with the mechanism of action of BRD4 inhibitors (32).

A dose-dependent decrease ($P < 0.01$) in c-MYC and TfR gene expression was also observed by quantitative RT-PCR in TNBC cells (MDA-MB-231 and MDA-MB-157) upon treatment with BRD4 inhibitors (Fig. 1). siRNA experiments (targeting c-MYC) corroborate that TfR is downregulated by MYC inhibition in these cell lines. Interestingly, a less aggressive (nontumorigenic in nude mice) TNBC cell line, Hs578T, showed a decrease in TfR gene expression while not actually affecting the c-MYC levels upon c-MYC siRNA transfection (Supplemental Fig. 2). However, both total MYC and total TfR protein were decreased in this cell line upon siRNA transfection at 48 h (Supplemental Fig. 2), suggesting evidence of either a mRNA rebound effect at the 24-h time point or a potentially false-negative siRNA result, as described by Holmes et al. (33).

The effects of BRD4 inhibitors on MYC and TfR protein expression in TNBC were interrogated via flow cytometry, internalization assay, and western blot (Supplemental Fig. 3). Surface expression of TfR was significantly decreased ($P < 0.001$) upon BRD4 treatment in MDA-MB-231 and MDA-MB-157 cells, as shown via flow cytometry. Radiolabeled (^{131}I) transferrin showed a 5%–10% decrease in internalization after drug treatment, when compared with vehicle-treated TNBC cells MDA-MB-231 and MDA-MB-157. Western blot also showed a decrease in MYC and TfR expression in MDA-MB-231 and MDA-MB-157 cells upon drug treatment, which can be seen both qualitatively and semiquantitatively through densitometry analysis in Supplemental Fig. 3. Hs578T cells were less responsive to BRD4 treatment at the protein level for most assays; however, densitometry analysis did show a decrease in the expression of MYC and TfR in Hs578T cells on drug treatment (Supplemental Fig. 3). A more transient internalization of ^{89}Zr-transferrin was observed over the course of 90 min in TNBC cells (Supplemental Fig. 4). MDA-MB-231 and MDA-MB-157 showed a significant internalization of ^{89}Zr-transferrin at 37°C, compared with the 4°C control, confirming receptor-mediated endocytosis in these cell lines. No statistical difference was noted between internalized fraction at 37°C versus 4°C in Hs578T cells, indicating less efficient internalization of transferrin in this cell line, since the highest percentage of bound radiotracer was found at the surface.

Radiolabeling ^{89}Zr-Transferrin

Purity and radiolabeling yields of ^{89}Zr-transferrin were quantified through instant thin-layer chromatography with a 50 mM ethylenediaminetetraacetic acid (pH 5) mobile phase (Supplemental Fig. 5). The radiochemical yield for each experiment ranged from 70% to 80%, and radiochemical purity was higher than 99% for all experiments. The specific activity
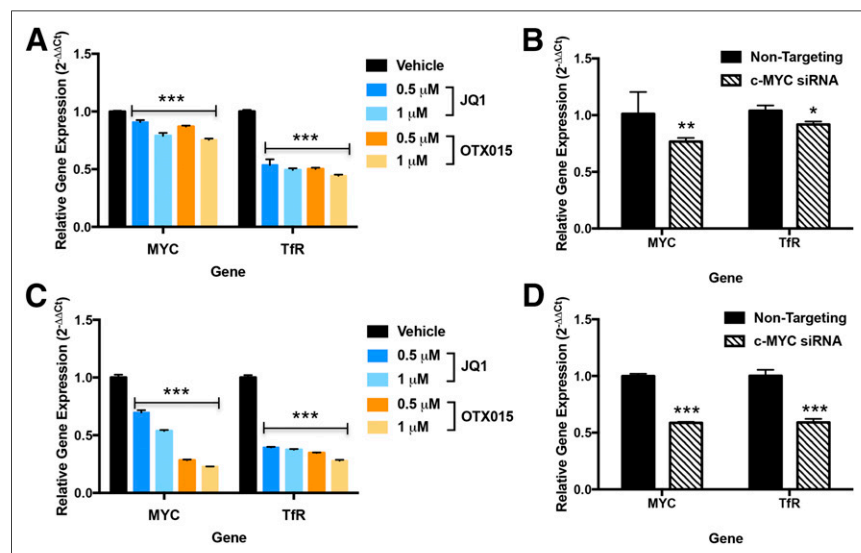

FIGURE 1. Assessing pharmacologic and transcriptional effects of BRD4 inhibitors and c-MYC siRNA transfection on MYC and TfR gene expression in TNBC cells. (A and B) In MDA-MB-231 cells, dose-dependent decrease in MYC and TfR gene expression is observed on BRD4 inhibition (A) and c-MYC siRNA knockdown (B). (C and D) In MDA-MB-157 cells, dose-dependent decrease in MYC and TfR gene expression is observed on BRD4 inhibition (C) and c-MYC siRNA knockdown (D). *$P < 0.05$. **$P < 0.01$. ***$P < 0.001$.
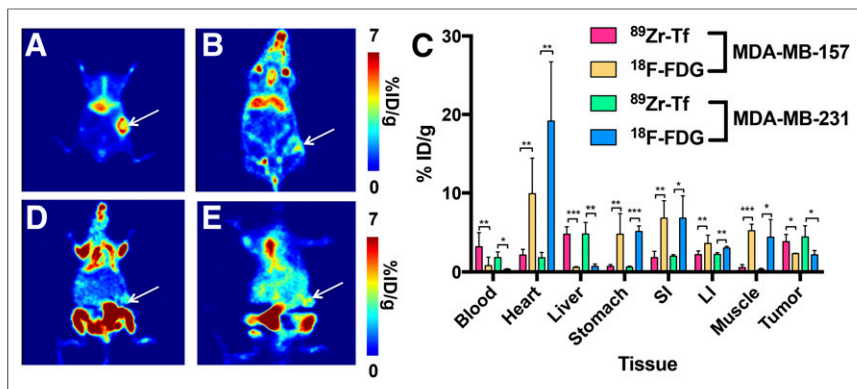
FIGURE 2. Representative PET images of ^{89}Zr-transferrin vs. ^{18}F-FDG uptake in mice bearing TNBC xenografts. (A and B) Coronal slices of ^{89}Zr-transferrin uptake at 48 h in MDA-MB-157 (A) and MDA-MB-231 (B) TNBC xenografts. (C) Biodistribution of ^{89}Zr-transferrin and ^{18}F-FDG uptake in select tissues of statistical significance in MDA-MB-231 and MDA-MB-157 tumor–bearing mice (n = 5/group). (D and E) Coronal slices of ^{18}F-FDG in MDA-MB-157 (D) and MDA-MB-231 (E) TNBC xenografts. *$P < 0.05$. **$P < 0.01$. ***$P < 0.001$. LI = large intestine; SI = small intestine.

of ^{89}Zr-transferrin ranged from 6 to 8 MBq/nmol for all experiments.

Exploring Uptake of ^{89}Zr-Transferrin Versus ^{18}F-FDG in Preclinical TNBC

We next tested whether TNBC models were avid for ^{89}Zr-transferrin in vivo by performing a head-to-head comparison of ^{89}Zr-transferrin and ^{18}F-FDG in a cohort of mice. The mice were kept fasting overnight and administered ^{18}F-FDG via tail vein injection, subsequently anesthetized, and imaged 1 h after injection. ^{89}Zr-transferrin uptake at 24 h was higher than ^{18}F-FDG uptake at 1 h in preclinical TNBC (MDA-MB-231), regardless of tumor size (Supplemental Fig. 6). Because of the noticeable difference in uptake between radiotracers, separate cohorts for more quantitative biodistribution studies were undertaken (Fig. 2), and mice were imaged at 1 h with ^{18}F-FDG and at 48 h with ^{89}Zr-transferrin using the same methods. Tumor uptake with ^{89}Zr-transferrin at 48 h was significantly higher ($P < 0.05$) than with ^{18}F-FDG at 1 h, on the basis of absolute uptake. A full biodistribution workup of ^{18}F-FDG versus ^{89}Zr-transferrin along with tumor-to-tissue ratios (for 1 h and 48 h for each radiotracer) can be found in Supplemental Tables 1 and 2.

Tumor uptake with ^{89}Zr-transferrin at 48 h was significantly higher ($P < 0.001$) than with ^{18}F-FDG at 1 h in the patient-derived xenograft TNBC model (Fig. 3). This result was quantified via regions of interest traced around the tumor
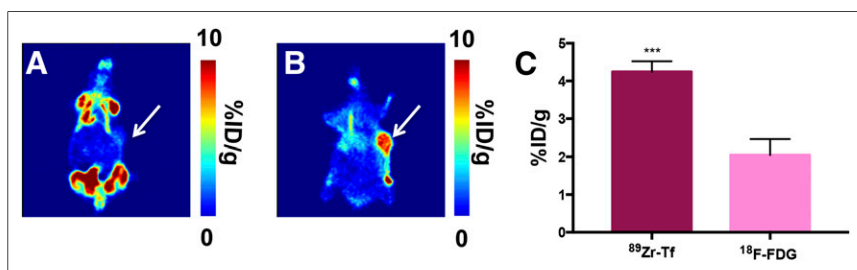

FIGURE 3. Uptake of ^{18}F-FDG vs. ^{89}Zr-transferrin in TNBC patient-derived xenograft tumor-bearing mice. (A and B) Coronal slice of ^{18}F-FDG uptake 1 h after injection (A) vs. ^{89}Zr-transferrin 48 h after injection (B). (C) Average tumor uptake of ^{89}Zr-transferrin uptake vs. ^{18}F-FDG based on regions of interest drawn around tumor for each radiotracer (n = 5). ***$P < 0.001$.

at multiple levels. Maximum-intensity projections, transverse images, and full biodistribution studies of ^{89}Zr-transferrin (at 48 h) can be found in Supplemental Figure 7. These results further support clinical translation of this ^{89}Zr-transferrin into TNBC patients, as ^{18}F-FDG is not as effective as ^{89}Zr-transferrin at tumor targeting in a highly clinically relevant model.

In vivo cohorts were repeated to implement extensive ex vivo analysis of TNBC tumors. Dual-isotope autoradiography showed differential uptake of ^{18}F-FDG and ^{89}Zr-transferrin in MDA-MB-231 and MDA-MB-157 tumors (Fig. 4). The tissues correlated well with uptake represented in the hematoxylin–eosin staining. Ex vivo immunohistochemistry confirmed TfR expression, compared with blocking peptide control, in paraffin-embedded tissues along with fresh-frozen tissue from the same cohort as used in the autoradiography. Additional ex vivo immunohistochemistry showed abundant c-MYC expression, compared with the IgG isotype control, supporting the known relationship between TfR and MYC expression (Supplemental Fig. 8).

DISCUSSION

All the presented data confirm that ^{89}Zr-transferrin is an improved radiotracer, compared with the clinical standard ^{18}F-FDG, and is able to better delineate tumors in preclinical TNBC. In addition to these exciting findings, we observed a robust effect of BRD4 inhibition of MYC and TfR at the proliferation, gene, and protein levels in tumorigenic basal-like TNBC cells, suggesting that TfR may be a useful biomarker to transiently interrogate therapy in MYC-overexpression cancers. BRD4 inhibitors induced cellular arrest at the G_0/G_1 phase at submicromolar concentrations in basal-like TNBC cells and were consistent with the previously reported literature (31). Hs578T cells were less sensitive than MDA-MB-231 and MDA-MB-157 cells at the protein level (MYC and TfR) via BRD4 inhibition. Hs578T cells have been described as metaplastic, encompassing a subset of breast cancer that may be more resistant to chemotherapy (34). This characteristic could explain the less pronounced pharmacologic response of Hs578T to BRD4 inhibitors at the protein level. Upon siRNA transfection of c-MYC, although Hs578T cells did not show an effect on c-MYC gene expression at the same concentration and time point as those that exhibited

sensitivity in the MDA-MB-231 and MDA-MB-157 cells, *TfR* gene expression was significantly decreased ($P < 0.05$). Also, western blot analysis in the same cohort of siRNA-transfected Hs578T cells shows that c-MYC siRNA transfection does in fact decrease c-MYC and TfR protein expression at 48 h (Supplemental Fig. 3). Further investigation of the pharmacologic and transcriptional effects in Hs578T cells to confirm these hypotheses is currently being pursued.

^{18}F-FDG was significantly less effective at tumor targeting than ^{89}Zr-transferrin ($P < 0.05$–0.001) in preclinical human TNBC, including a patient-derived xenograft model
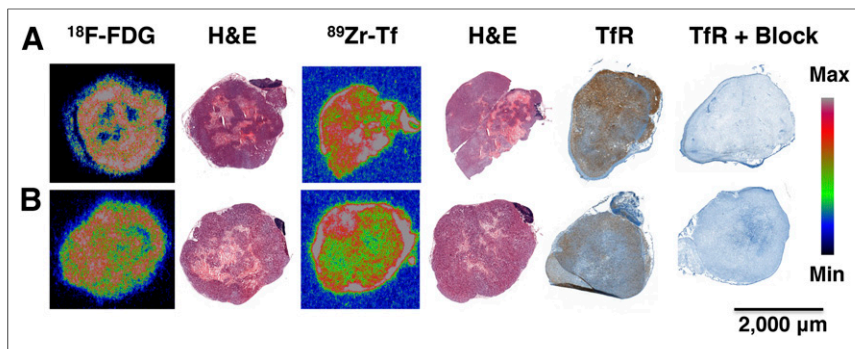
FIGURE 4. Dual-isotope autoradiography of ^{18}F-FDG and [89]Zr-transferrin uptake and subsequent histology and immunohistochemistry of MDA-MB-231 (A) and MDA-MB-157 (B) TNBC tumors. Expression of TfR correlates with [89]Zr-transferrin uptake and can be blocked with control peptide (10-fold excess). Same level of fresh frozen tissue is illustrated in each tumor type (n = 3/group). All tissue is shown at 1× magnification at 2,000 μm. Heat map scale bar represents minimum and maximum values for autoradiography. H&E = hematoxylin–eosin.

epidermal growth factor receptor (*40,43*), and protooncogene serine/threonine-protein kinase pathway (*44*).

CONCLUSION

Establishing biomarkers within heterogeneous cancers such as TNBC fulfills a clinically unmet need to reliably annotate tumor uptake or treatment response. [89]Zr-transferrin targets human TNBC primary tumors significantly better than ^{18}F-FDG, as shown through PET imaging and biodistribution studies. [89]Zr-transferrin is a useful tool to interrogate MYC via TfR-targeted PET imaging in TNBC. These data could lead to investigations of oncogenic pathways and uncover druggable biomarkers within TNBC.

(Figs. 2 and 3). The uptake of our tracer in 3 preclinical models (MDA-MB-231, MDA-MB-157, and a TNBC patient-derived xenograft) confirms our hypothesis that detecting MYC status could be improved using our radiotracer. Ex vivo autoradiography shows differential uptake of ^{18}F-FDG and [89]Zr-transferrin in MDA-MB-231 and MDA-MB-157 tumors (Fig. 4). Tissue is shown side by side with respective hematoxylin–eosin stainings, confirming uptake in cancerous tissue. In addition, [89]Zr-transferrin uptake correlates with both hematoxylin–eosin and anti-TfR antibody, confirming both tumor-specific and protein-specific uptake in TNBC. Immunohistochemistry in these same tissues confirms c-MYC and TfR protein expression in TNBC tumors, compared with IgG isotype and blocking control (Supplemental Fig. 8), verifying the link between MYC and TfR overexpression in TNBC.

MYC and TfR are targets for therapy and imaging, respectively, and have the capacity to identify more than just the hypermetabolism of TNBC, which can be imaged by ^{18}F-FDG. Noninvasive imaging using [89]Zr-transferrin can aid in further annotating these oncogenes and their role in tumorigenesis. The ability of [89]Zr-transferrin to successfully target TNBC preclinically shows promise for the utility of this probe to further select patients for novel therapeutics.

There is a clinically unmet need to establish and detect biomarkers within TNBC. TNBC responds unpredictably to chemotherapy and radiation therapy, making it the most challenging prognosis within breast cancer. Multiple targets and drugs are being explored to uncover biomarkers in TNBC to improve the prognosis of this challenging malignancy. PET imaging techniques have evolved for other subtypes of breast cancer, particularly those that overexpress HER2 (*35*). These techniques together, in addition to, or instead of metabolic imaging with ^{18}F-FDG, can better select patients for therapy or gauge disease response. [89]Zr-transferrin might also be used to assess mammalian-target-of-rapamycin signaling (*29*), another candidate for inhibitor therapy within TNBC (*1,36,37*).

New avenues for molecular imaging could change the way TNBC is approached, improving the current standard of ^{18}F-FDG PET. MYC has been established as a relevant biomarker within TNBC (*2,38*). Multiple signaling molecules closely tied to MYC are relevant in TNBC, namely the phosphatidylinositol-3-kinase pathway (*39–41*), mitogen-activated protein kinase (*42*),

REFERENCES

1. Crown J, O'Shaughnessy J, Gullo G. Emerging targeted therapies in triple-negative breast cancer. *Ann Oncol.* 2012;23(suppl 6):vi56–vi65.
2. Horiuchi D, Kusdra L, Huskey NE, et al. MYC pathway activation in triple-negative breast cancer is synthetic lethal with CDK inhibition. *J Exp Med.* 2012;209:679–696.
3. Shen L, O'Shea JM, Kaadige MR, et al. Metabolic reprogramming in triple-negative breast cancer through Myc suppression of TXNIP. *Proc Natl Acad Sci USA.* 2015;112:5425–5430.
4. Green AR, Aleskandarany MA, Agarwal D, et al. MYC functions are specific in biological subtypes of breast cancer and confers resistance to endocrine therapy in luminal tumours. *Br J Cancer.* 2016;114:917–928.
5. Dang CV. MYC, Metabolism, cell growth, and tumorigenesis. *Cold Spring Harb Perspect Med.* 2013;3:a014217–a014232.

6. Vander Heiden MG, Cantley LC, Thompson CB. Understanding the Warburg effect: the metabolic requirements of cell proliferation. *Science.* 2009;324:1029–1033.

7. Palaskas N, Larson SM, Schultz N, et al. ^{18}F-fluorodeoxy-glucose positron emission tomography ([18]FDG-PET) marks MYC-overexpressing human basal-like breast cancers. *Cancer Res.* 2011;71:5164–5174.

8. Warburg O. On the origin of cancer cells. *Science.* 1956;123:309–314.

9. Yu S. Review of ^{18}F-FDG synthesis and quality control. *Biomed Imag Interv J.* 2006;2:e57–e68.

10. Surasi DS, Bhambhvani P, Baldwin JA, Almodovar SE, O'Malley JP. ^{18}F-FDG PET and PET/CT patient preparation: a review of the literature. *J Nucl Med Technol.* 2014;42:5–13.

11. Zhuang H, Chacko T, Hickeson M, et al. Persistent non-specific FDG uptake on PET imaging following hip arthroplasty. *Eur J Nucl Med Mol Imaging.* 2002;29:1328–1333.

12. Shreve PD, Anzai Y, Wahl RL. Pitfalls in oncologic diagnosis with FDG PET imaging: physiologic and benign variants. *Radiographics.* 1999;19:61–77.

13. Long NM, Smith CS. Causes and imaging features of false positives and false negatives on ^{18}F-PET/CT in oncologic imaging. *Insights Imaging.* 2011;2:679–698.

14. Park JS, Yim J-J, Kang WJ, et al. Detection of primary sites in unknown primary tumors using FDG-PET or FDG-PET/CT. *BMC Res Notes.* 2011;4:56–62.

15. Jadvar H, Alavi A, Gambhir SS. ^{18}F-FDG uptake in lung, breast, and colon cancers: molecular biology correlates and disease characterization. *J Nucl Med.* 2009;50:1820–1827.

16. Vander Heiden MG. Targeting cancer metabolism: a therapeutic window opens. *Nat Rev Drug Discov.* 2011;10:671–684.

17. Abo-Sheisha DM, Badawy ME. The diagnostic value of PET/CT in recurrence and distant metastasis in breast cancer patients and impact on disease free survival. *Egyptian J Rad Nucl Med.* 2014;45:1317–1324.

18. Groheux D, Majdoub M, Sanna A, et al. Early metabolic response to neoadjuvant treatment: FDG PET/CT criteria according to breast cancer subtype. *Radiology.* 2015;277:358–371.

19. Vercher-Conejero JL, Pelegrí-Martinez L, Lopez-Aznar D, Cózar-Santiago MP. Positron emission tomography in breast cancer. *Diagnostics (Basel).* 2015;5:61–83.

20. Shibuya K, Yoshida E, Nishikido F, et al. Limit of spatial resolution in FDG-PET due to annihilation photon non-collinearity. In: Magjarevic R, Nagel JH, eds. *World Congress on Medical Physics and Biomedical Engineering 2006 (IFMBE Proceedings, Vol 14).* New York, NY: Springer; 2007:1667–1671.

21. Chang JM, Lee HJ, Goo JM, et al. False positive and false negative FDG-PET scans in various thoracic diseases. *Korean J Radiol.* 2006;7:57–69.

22. Dashevsky BZ, Goldman DA, Parsons M, et al. Appearance of untreated bone metastases from breast cancer on FDG PET/CT: importance of histologic subtype. *Eur J Nucl Med Mol Imaging.* 2015;42:1666–1673.

23. Daniels TR, Bernabeu E, Rodríguez JA, et al. Transferrin receptors and the targeted delivery of therapeutic agents against cancer. *Biochim Biophys Acta.* 2012;1820:291–317.

24. Holland JP, Evans MJ, Rice SL, Wongvipat J, Sawyers CL, Lewis JS. Annotating MYC oncogene status with [89]Zr-transferrin imaging. *Nat Med.* 2012;18:1586–1591.

25. Torti SV, Torti FM. Cellular iron metabolism in prognosis and therapy of breast cancer. *Crit Rev Oncog.* 2013;18:435–448.

26. Habashy HO, Powe D, Staka C, et al. Transferrin receptor (CD71) is a marker of poor prognosis in breast cancer and can predict response to tamoxifen. *Breast Cancer Res Treat.* 2010;119:283–293.

27. Evans MJ, Holland JP, Rice SL, et al. Imaging tumor burden in the brain with [89]Zr-transferrin. *J Nucl Med.* 2013;54:90–95.

28. Doran MG, Carnazza KE, Steckler JM, et al. Applying [89]Zr-transferrin to study the pharmacology of inhibitors to BET bromodomain containing proteins. *Mol Pharm.* 2016;13:683–688.

29. Truillet C, Cunningham JT, Parker MFL, et al. Non-invasive measurement of mTORC1 signaling with [89]Zr-transferrin. *Clin Cancer Res.* 2017;23:3045–3052.

30. Holland JP, Sheh Y, Lewis JS. Standardized methods for the production of high specific-activity zirconium-89. *Nucl Med Biol.* 2009;36:729–739.

31. Shu S, Lin CY, He HH, et al. Response and resistance to BET bromodomain inhibitors in triple-negative breast cancer. *Nature.* 2016;529:413–417.

32. Chaidos A, Caputo V, Karadimitris A. Inhibition of bromodomain and extra-terminal proteins (BET) as a potential therapeutic approach in haematological malignancies: emerging preclinical and clinical evidence. *Ther Adv Hematol.* 2015;6:128–141.

33. Holmes K, Williams CM, Chapman EA, Cross MJ. Detection of siRNA induced mRNA silencing by RT-qPCR: considerations for experimental design. *BMC Res Notes.* 2010;3:53–58.

34. Chavez KJ, Garimella SV, Lipkowitz S. Triple negative breast cancer cell lines: one tool in the search for better treatment of triple negative breast cancer. *Breast Dis.* 2010;32:35–48.

35. Henry KE, Ulaner GA, Lewis JS. HER2-targeted PET/SPECT imaging of breast cancer: non-invasive measurement of a biomarker integral to tumor treatment and prognosis. *PET Clin.* 2017;12:269–288.

36. Lee JJX, Loh K, Yap Y-S. PI3K/Akt/mTOR inhibitors in breast cancer. *Cancer Biol Med.* 2015;12:342–354.

37. Yunokawa M, Koizumi F, Kitamura Y, et al. Efficacy of everolimus, a novel mTOR inhibitor, against basal-like triple-negative breast cancer cells. *Cancer Sci.* 2012;103:1665–1671.

38. Camarda R, Zhou AY, Kohnz RA, et al. Inhibition of fatty acid oxidation as a therapy for MYC-overexpressing triple-negative breast cancer. *Nat Med.* 2016;22:427–432.

39. Lehmann BD, Bauer JA, Chen X, et al. Identification of human triple-negative breast cancer subtypes and preclinical models for selection of targeted therapies. *J Clin Invest.* 2011;121:2750–2767.

40. Yi YW, Hong W, Kang HJ, et al. Inhibition of the PI3K/AKT pathway potentiates cytotoxicity of EGFR kinase inhibitors in triple-negative breast cancer cells. *J Cell Mol Med.* 2013;17:648–656.

41. Britten CD. PI3K and MEK inhibitor combinations: examining the evidence in selected tumor types. *Cancer Chemother Pharmacol.* 2013;71:1395–1409.

42. Giltnane JM, Balko JM. Rationale for targeting the Ras/MAPK pathway in triple-negative breast cancer. *Discov Med.* 2014;17:275–283.

43. Maiello MR, D'Alessio A, Bevilacqua S, Gallo M, Normanno N, De Luca A. EGFR and MEK blockade in triple negative breast cancer cells. *J Cell Biochem.* 2015;116:2778–2785.

44. Brasó-Maristany F, Filosto S, Catchpole S, et al. PIM1 kinase regulates cell death, tumor growth and chemotherapy response in triple-negative breast cancer. *Nat Med.* 2016;22:1303–1313.